Journal of Power Sources 246 (2014) 679–695

Contents lists available at ScienceDirect

Journal of Power Sources

journal homepage: www.elsevier.com/locate/jpowsour

Numerical simulations of water droplet dynamics in hydrogen fuel cell gas channel

Hyo-Yup Kim, Segye Jeon, Myeongho Song, Kyoungyoun Kim*

Department of Mechanical Engineering, Hanbat National University, Daejeon 305-719, South Korea

HIGHLIGHTS

- We investigated the droplet dynamics from two pores, using a 3D VOF model.
- Hydrophilic sidewall shows more effective fuel transport to the reaction site.
- Clogging was more likely to occur for hydrophobic channel wall.

ARTICLE INFO

Article history:
Received 25 May 2013
Received in revised form
3 August 2013
Accepted 8 August 2013
Available online 20 August 2013

Keywords:
Fuel cell
Water droplet
Two-phase flow
Computational fluid dynamics
Volume of fluid
Pressure drop

ABSTRACT

The droplet dynamics in the cathode gas flow channel of a hydrogen fuel cell has been numerically investigated to obtain ideas for designing a flow channel to effectively prevent flooding. Three-dimensional two-phase flow simulations employing the volume of fluid method have been performed. Liquid droplets emerging from two adjacent pores at the hydrophobic bottom wall are subjected to airflow in the bulk of the gas flow channel. The effects of various parameters (pore distance, locations, sidewall contact angle, and airflow rate) on the liquid water removal from the gas channel have been investigated in terms of liquid water saturation, coverage of liquid water on the gas diffusion layer (GDL) surface, and change in the pressure drop in the channel. The numerical results show that the coalescence of two adjacent droplets enhances the water removal as compared to two separate, small droplets. It is also observed that droplets generated near the hydrophilic sidewall can be attached to the upper corner of the channel walls, which prevents the liquid water from covering the GDL surface, whereas the hydrophobic sidewall may cause clogging of the gas channel with liquid water at a low airflow rate.

© 2013 Elsevier B.V. All rights reserved.

1. Introduction

A polymer electrolyte membrane fuel cell (PEMFC) has a wide range of applications because of its diverse advantages, including high power density, relatively simple structure, rapid start-up and response capability, and excellent durability in comparison to other types of fuel cells. Further, it has attracted considerable attention as an attractive source of clean energy because of its electrochemical mechanism capable of generating electrical power directly from an electrochemical process. In addition to electricity, a PEMFC produces water as a byproduct. Water is generated through the electrochemical reaction between the oxygen fed through the gas flow channel and the hydrogen ions traveling through the electrolyte, whereby flooding may result from an inadequate liquid water discharge in the channel, thus impeding the fuel transport to the reaction site and leading to problems of diminished fuel cell function. Therefore, to improve the PEMFC performance, it is important to control and manage the water generated during the electrochemical process.

From this perspective, the study of the droplet behaviors in the gas flow channel is of vital importance for enhancing fuel cell performance, and hence, related research has been conducted extensively. Table 1 lists several recent experimental studies on liquid water behaviors in a fuel cell gas channel (GC). Most studies have been performed using a transparent fuel cell to visualize the liquid water behavior in the flow channel. Zhang et al. [1] showed different flow patterns of liquid water for airflow rates in the gas channel and reported that the corner flow pattern leads to efficient water removal from the gas channel with a relatively low parasitic power. Ous et al. [2] investigated the effects that the operating conditions of a transparent PEMFC, such as reactant stoichiometry,

* Corresponding author. Tel.: +82 42 821 1077; fax: +82 42 821 1587.
E-mail address: kkim@hanbat.ac.kr (K. Kim).

0378-7753/$ – see front matter © 2013 Elsevier B.V. All rights reserved.
http://dx.doi.org/10.1016/j.jpowsour.2013.08.032

Nomenclature

A	area (m^2)
A_w	relative coverage of liquid water on the GDL surface
d	droplet diameter (m)
F	force (N), momentum source ($N\ m^{-3}$)
g	gravitational acceleration ($m\ s^{-2}$)
H	channel height (m)
n	unit normal vector
p	pressure (Pa)
R_{dp}	relative change in the pressure drop in the gas channel
S_w	liquid water saturation in the gas channel
t	time (s)
V	velocity ($m\ s^{-1}$)

Greek letters

α	volume fraction
δ	distance (m)
κ	local curvature of the interface surface (m^{-1})
μ	viscosity ($kg\ (m\ s)^{-1}$)
θ	contact angle (rad, °)
ρ	density ($kg\ m^{-3}$)
σ	surface tension ($N\ m^{-1}$)

Subscript

0	single phase flow
d	drag
k	fluid index
w	water, wall

cell temperature, and electric load, have on the liquid water formation and extraction in serpentine flow channels. Further, Hsieh et al. [3] examined different channel configurations in addition to diverse operating conditions and reported that a uniform current distribution may be obtained in an interdigitated flow channel despite a considerable pressure drop. Zhan et al. [4] conducted an in-depth study on water transport, taking into account the operating conditions, including current density, temperature, air stoichiometry, and relative humidity. On the other hand, there was a study investigating, along with the water transport in an active fuel cell, the dynamic evolution of a water droplet by feeding water from a pore at a predetermined velocity [5].

In parallel with experimental studies, a number of studies based on numerical simulation have also been carried out (Table 2). Most studies have revolved around the GC or PEMFC cathode [6–17], and of late, there have been studies investigating the liquid water transport in the PEMFC itself including the membrane electrode assembly (MEA) and the gas diffusion layer (GDL) [18–20]. Some such studies included a simulation of the conditions in which liquid water is gradually fed from the GDL pore to GC [9,12–14], whereas others involved a simulation with a given liquid water distribution as the initial condition [6–8,18]. Therein, a smooth hydrophobic surface was used as the GC bottom surface to express the GDL, and a hydrophilic condition was provided for the top and sidewall surfaces of the GC. Chen et al. [9] went further and introduced a hybrid structure model cube simulating a realistic GDL structure. The majority of these studies focused on the liquid water dynamics from the perspective of fluid dynamics, and some recent papers conducted in-depth studies on the coupled process of liquid water transport and reactant transfer [9,15,19]. According to their study results, the transport of liquid water in the GC follows the route of the droplets generated from the pores as they are detached from pores and travel at the airflow rate; this process is influenced by the channel design and the channel surface. Further, factors influencing the liquid water dynamics in the GC are very diverse, such as operating conditions, geometrical shapes of the channel, and the interactions among droplets.

However, most of the existing studies on the droplet behaviors in a channel are limited to a single droplet generated from a single pore in the channel, and the mechanism of inter-droplet interaction is difficult to understand. Moreover, there is a lack of studies closely investigating the interaction between multiple droplets and the channel wall. Therefore, this study investigated the inter-droplet interactions under the condition of discharging water from two pores into the airflow stream of the cathode channel, using a 3D volume of fluid (VOF) model. The droplet dynamics was analyzed in the spatiotemporal context with respect to various cases dependent on the distance between the pores, distance from the gas channel sidewall, contact angle of sidewalls, and airflow rate change. Further, a comparative analysis was carried out on the liquid water saturation and the liquid water coverage on the GDL surface in the channel and on the time-dependent change in the pressure drop.

2. Computational details

The flow in the GC was assumed as being unsteady, isothermal, and laminar 3D flows, with negligible heat generation and heat transfer. This study employed a VOF model of a two-phase flow. VOF is a surface-tracking method employed to study the location of the interface between two unmixable fluids. The equations governing the two-phase fluid flow are the continuity equation and the Navier–Stokes equation expressed as follows:

$$\frac{\partial \rho}{\partial t} + \nabla \cdot (\rho \mathbf{V}) = 0, \tag{1}$$

Table 1
Experimental studies on droplet dynamics in fuel cell gas channels.

Authors and published year	GC shape	Research aspects	Condition
Zhang et al., 2006	Transparent PEFC	Effects of gas flow velocity on water droplet dynamic behaviors	Electrochemical reaction
Ous et al., 2009	Transparent PEMFC	Effect of air stoichiometry, hydrogen stoichiometry, temperature, and electric road on the accumulation of liquid water in PEMFC flow channels	Electrochemical reaction
Hsieh et al., 2011	Four different flow channels	Effects of pressure drop, hydrogen, airflow rates, cell temperatures, water accumulation, and current density distribution on the cathode of a PEMFC	Electrochemical reaction
Zhan et al., 2012	Transparent PEMFC	Transport process of liquid water with different operating conditions	Electrochemical reaction
Wu et al., 2012	Transparent channel with water inlet pore	Flow regimes under different air and water velocities; effect of air velocity on the dynamic contact angle of the droplet	Injection of water from a small pore

Table 2
Numerical studies on droplet dynamics in fuel cell gas channels.

Authors and published year	No. of pores	Pore size [μm]	GC shape	GC dimensions (height × width × length) [mm]	Method	Research aspects	Conditions
Jiao et al., 2006			Straight micro-parallel-channels with manifolds	0.2 × 0.2 × 0.5	VOF	Behaviors of liquid water with different initial water distribution	Different initial liquid water distribution
Zhu et al., 2007	1 or 2	50	Single rectangle GC with water inlet pore	0.25 × 1	VOF	Effects of GC size, inlet pore size, coalescence of water droplets, and air velocity on liquid water behaviors	2D flow
Zhu et al., 2008	1	50	Single square GC with water inlet pore	0.25 × 0.25 × 1	VOF	Effects of static contact angle, air inlet velocity, water injection velocity, and pore size on water droplet dynamic behaviors	3D flow
Hao et al., 2009	1	90	Single rectangle GC with water inlet pore	0.3 × 0.3 × 1.2	LBM	Effects of gas flow velocity and GDL wettability on water droplet dynamic behavior	A water droplet emerging through a micro-pore on GDL surface with different contact angle
Akhtar et al., 2011			Single tapered rectangular GC without water inlet pore	Inlet (1 × 1) Outlet (0.5 × 1)	Level-set (FEM)	Effect of tapering the channel downstream and wall wettability on liquid water behavior	Initial liquid water droplet
Carton et al., 2011			Double serpentine GC		VOF experimental	Coalescence of droplets and movement of water slugs in flow field mini-channels	Initial liquid water droplet
Han et al., 2012	2	30	Single rectangle GC with water inlet pore	0.5 × 0.5 × 1	LBM	Effects of gas flow velocity, pore size, pore distances, and GDL wettability on liquid droplet transport behaviors	2D flow
Cho et al., 2012			Single rectangular GC without water inlet pore	1 × 1.8 × 23	VOF	Analytical model for critical gas velocity	Initial liquid water droplet
Qin et al., 2012	3	50, 40	Single rectangular GC with water inlet pore	0.25 × 0.5 × 1	VOF	Effects of gas flow rate, GDL wettability, and sidewall contact angle on water droplet dynamics	Liquid water is transported from a water reservoir to the GC by three cylindrical pipes
Chen et al., 2012	1	60	Hybrid GDL with water inlet pore		VOF	Effect of air inlet velocities and GC wall wettability on liquid water behaviors, mass transport, and current density distribution	Coupled process of liquid water transport and reactant transfer
Ding et al., 2013	20	250	Single straight square GC with water inlet pore	1 × 1 × 100	VOF	Effects of two-phase flow patterns, liquid generation rates, current densities, gas stoichiometric flow ratios, and surface wettabilities on the PEM fuel cell performance	3D VOF coupling with a 1D MEA model
Hossain et al., 2013	10–39,	50, 20	Single square GC with water inlet pore	0.25 × 0.25 × 1	VOF	Effects of different pore distances and pore sizes on water droplet dynamics	Multiple pores on the GDL surface

$$\frac{\partial \rho \mathbf{V}}{\partial t} + \nabla \cdot (\rho \mathbf{V}\mathbf{V}) = -\nabla p + \nabla \cdot \left(\mu \left(\nabla \mathbf{V} + \nabla \mathbf{V}^T \right) \right) + \rho \mathbf{g} + \mathbf{F}, \tag{2}$$

where p represents the pressure; ρ and μ represent the volume-averaged density and viscosity, respectively; $\mathbf{V}$ represents the fluid flow rate; and $\mathbf{g}$ represents the gravitational acceleration. $\mathbf{F}$ represents the surface tension momentum source term and is expressed, according to the continuum surface force model [21], as follows:

$$\mathbf{F} = \sigma \kappa_k \frac{\rho \nabla \alpha_k}{\langle \rho \rangle}, \tag{3}$$

where σ is the surface tension coefficient, $<\rho>$ is the averaged density of the two fluids, and κ_k denotes the local curvature of the interface surface, as expressed in

$$\kappa_k = \nabla \cdot \mathbf{n}, \tag{4}$$

where $\mathbf{n}$ is the interface surface normal vector ($\mathbf{n} = \nabla \alpha_k / \nabla \alpha_k$).

The volume fraction α_k is calculated in each single computational cell throughout the entire domain by computing the volume fraction of fluid k. $\alpha_k = 0$ implies that the computational cell does not contain any kth fluid; $0 < \alpha_k < 1$ implies that the computational cell is partially filled with the kth fluid; and $\alpha_k = 1$ implies that the computational cell is completely filled with the kth fluid. The sum total of the volume fraction functions of all fluids is equal to 1. α_k is governed by the following volume fraction equation, which is solved in every computational cell:

$$\frac{\partial \alpha_k}{\partial t} + \mathbf{V} \cdot \nabla \alpha_k = 0 \tag{5}$$

The wall adhesion is taken into account by implying the unit normal vector of the interface surface at the wall as

$$\mathbf{n} = \mathbf{n_w} \cos\theta + \mathbf{t_w} \sin\theta, \tag{6}$$

where $\mathbf{n_w}$ and $\mathbf{t_w}$ are unit vectors normal and tangential to the solid wall, respectively, and θ is the contact angle.

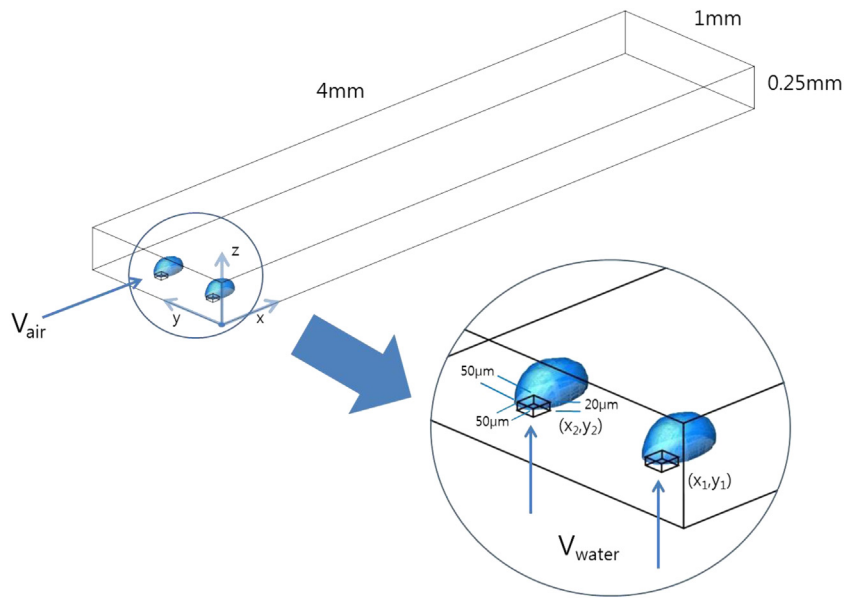

Fig. 1. Computational domain.

By using the VOF model, the present study examines the dynamics of liquid water droplets which emerge from two adjacent pores at the GDL surface and are subjected to airflow in the bulk of the cathode gas flow channel. Fig. 1 shows the 3D computational domain used in this study. A case was assumed where two pores measuring 50 μm × 50 μm were installed in a channel having a quadrangular cross section of 1 mm × 0.25 mm and a streamwise length of 2 mm. Since the main focus of the present study is to investigate the water droplet dynamics in the gas channel, the computational domain was chosen as the gas flow channel with a hydrophobic bottom wall which corresponds to the surface of GDL. However, it is also important to examine the water droplet dynamics inside the pores in GDL because flooding mainly occurs in the cathode side GDL and catalyst layer. Table 3 lists in detail the geometrical and physical properties of the channel flow configuration. Table 4 lists the flow conditions for the test cases of the present study. V_{air} and V_{water} denote the velocity of air at the channel inlet and that of the liquid water supply from the pores, respectively. As shown in Fig. 1, the relative locations of the pores, (x_1, y_1) and (x_2, y_2) indicate the locations of the two pores with respect to the origin (0, 0). The channel bottom, corresponding to the GDL surface, was hydrophobic and had the same contact angle (θ_{bottom}) of 110° for all the test cases, but the contact angle ($\theta_{channel}$) of the sidewall was designed to vary. Table 5 presents a dimensionless number for each case (Re_{gs}, We_{gs}, and Bd). The relatively low value of Bd suggests that the surface tension force is more influential than the gravitational force, and consequently, the surface tension force in the channel plays a crucial role in determining the droplet behavior.

The boundary conditions for the air inlet and the water inlet were given by prefixed velocities in Table 4, and the outflow condition was applied to the outlet. The boundary condition except for the inlet and the outlet was determined to be a no-slip condition. In all, 36,260,000 cells of the computational grid were used for the calculation. The governing equations are solved by the pressure–velocity coupling method through the PISO scheme and the interface tracking between gas–liquid through a geometric reconstruct scheme. In this scheme, the interface between air and water is determined by a piecewise linear interface calculation method. Further details on numerical method can be found in Ref. [22].

Table 3
Geometrical and physical parameters.

Parameters	Value
GC width/height/length	1/0.25/4 mm
Pore size	50 μm × 50 μm
Gas density (ρ_{air})	1.225 kg m^{-3}
Liquid water density (ρ_{water})	998.2 kg m^{-3}
Gas dynamic viscosity	1.7894 × 10^{-5} kg (m s)$^{-1}$
Liquid water dynamic viscosity	0.001003 kg (m s)$^{-1}$
Surface tension (σ)	0.0728 N m^{-1}

3. Results

Figs. 2–9 show the spatiotemporal evolutions of liquid water droplets in the gas flow channels for each case listed in Table 4. Liquid water droplets are visualized using the isosurface of $\alpha_w = 0.1$. Further, the temporal variations in liquid water saturation in the gas channel (S_w) and the relative coverage of liquid water on the GDL surface (A_w) are examined to quantify the water droplet behaviors, which are defined as below, respectively:

$$S_w = \frac{1}{V_{channel}} \int \alpha_w dV \tag{7}$$

$$A_w = \frac{1}{A_{bottom}} \int \alpha_w dA \tag{8}$$

Fig. 2 shows the droplet growth and the water discharge patterns when liquid water is inlet from two pores that are horizontally 0.4 mm apart (Case 1). Because of the relatively large distance between the pores, two droplets grow independently of each other (Fig. 2a–e) and travel adrift separately from their respective pores (Fig. 2f); however, they are discharged without adhering to the channel sidewall (Fig. 2i).

Table 4
Simulation cases.

Case	V_{air} [m s^{-1}]	V_{water} [m s^{-1}]	(x_1,y_1) [mm]	(x_2,y_2) [mm]	$\theta_{channel}$ [deg.]
1	10	0.02	(0.2,0.3)	(0.2,0.7)	45
2	10	0.02	(0.2,0.45)	(0.3,0.45)	45
3	10	0.02	(0.2,0.1)	(0.3,0.1)	45
4	2	0.02	(0.2,0.45)	(0.3,0.45)	45
5	2	0.02	(0.2,0.1)	(0.3,0.1)	45
6	2	0.02	(0.2,0.45)	(0.3,0.45)	110
7	5	0.02	(0.2,0.45)	(0.3,0.45)	110

Fig. 3 shows the condition (Case 2) where the pores are 0.1 mm apart in the streamwise direction. Because of the relative proximity of the two pores, the two droplets grow as a single droplet coalesced in an earlier phase of growth (Fig. 3b) and travel apart later on (Fig. 3h); however, they are discharged as water without adhering to the channel sidewall (Fig. 3i).

However, in Case 3 (Fig. 4), where the pores are positioned near the sidewall, a droplet growth pattern similar to the one in Case 2 is observed in an earlier growth phase; the detachment from the pores (Fig. 4a–e) also occurs during this phase. However, adhesion to the hydrophilic channel wall takes place immediately thereafter (Fig. 4f), and the water is discharged along the channel edge (Fig. 4h).

On the other hand, Fig. 5 shows the droplet growth and the water discharge patterns when the pores are positioned at the channel center and the inlet velocity is slightly low (Case 4). Although the two droplets are coalesced and grow together in an earlier growth phase (Fig. 5b), they are not separated because of the low inlet air velocity; instead, they adhere to the top wall (Fig. 5c). As soon as the mature droplet adheres to the top wall, it is separated (Fig. 5d) and the water is discharged along the top wall (Fig. 5e–i).

Further, Fig. 6 shows Case 5, wherein the inlet velocity is low and the pores are positioned close to a sidewall; here, a droplet adheres to the sidewall during growth (Fig. 6c) unlike in Case 3 where a droplet adheres to the sidewall immediately after detachment from the pores, and the water is discharged along a channel edge (Fig. 6i).

Fig. 7 shows a condition having a hydrophobic channel wall surface and a low inlet velocity (Case 6), wherein the droplets show an early-phase growth pattern similar to the that in Case 4 with a hydrophilic channel wall but touch the top wall without being separated because of the low inlet velocity (Fig. 7d). Nevertheless, as the channel wall surface is hydrophobic, they do not spread but show a clogging pattern (Fig. 7e–j). However, because of an inlet velocity (Case 7) greater than that in Case 6, the mature droplets (Fig. 8a–g) do not adhere to the top wall but are detached from the pores (Fig. 8h) and discharged as water (Fig. 8i–j).

Thus far, we have qualitatively observed the droplet growth and water discharge patterns, as shown in Figs. 2–8. Figs. 9–13 show the quantitative changes in S_w, A_w, and R_{dp} under different flow conditions, whereby the relative change in the pressure drop (R_{dp}) between the inlet and the outlet of the gas channel is defined as follows:

$$R_{dp} = \frac{\Delta P - \Delta P_0}{\Delta P_0}, \tag{9}$$

where ΔP and ΔP_0 denote the pressure drop when a droplet is present and absent, respectively, and ΔP_0 was calculated by performing additional single phase flow simulations.

Because the pores, through which water passes from the GDL in the channel, are randomly generated during real PEMFC operations, the inter-pore distance is not regular. This implies that the pores can be positioned relatively more or less apart as well as near the channel wall surface. Fig. 9 shows the effects of variations in the pore position according to the changes in S_w, A_w, and R_{dp} in the GC. Fig. 9a shows the temporal variations of water saturation (S_w) in the channel; it increases in an earlier phase, followed by an abrupt decrease, and a repetitive pattern of increase and decrease. The gradients for S_w increase phases are identical for three cases because of the same water flow amount inlet through the pores. Each instant at which an abrupt decrease occurs is the moment when the water in the channel begins to discharge through the channel outlet. Moreover, whereas the S_w decreasing gradients are steep in Case 1 and Case 2, that in Case 3 are considerably less steep. This feature in Case 3 is attributed to the water discharge through the channel outlet alongside a hydrophilic edge (Fig. 4), which decelerates the outlet velocity as compared to the discharge alongside the hydrophobic bottom wall. Fig. 9b shows the change in the ratio (A_w) of the GDL surface covered by the liquid water to the entire GCL area in time series. It shows a repetitive increase–decrease pattern similar to that of S_w. In Case 1 and Case 2, A_w and S_w were decreased at the same instant, whereas the instant of A_w decrease was observed earlier than that of S_w decrease in Case 3. This is because in this case, droplets are attached to the sidewall prior to the water discharge through the channel outlet, resulting in a relatively reduced coverage of the bottom surface (Fig. 4). Moreover, as shown in Fig. 9c, the change pattern of the relative amount of pressure drop R_{dp} triggered by the droplets is closer to A_w than to S_w, which suggests that the pressure drop is more dependent on the change in effective surface than amount of liquid water inside the GC. Taken together, these results show that the closer the inter-pore distance, the smaller is the S_w and the faster is the water discharge, and the comparison of A_w representing the portion of GDL surface coverage evidences the effectiveness of hydrophilic sidewall for liquid water removal from the GDL surface.

Water discharge in the GC is crucial for the prevention of clogging, and a sufficiently high airflow velocity is required to this effect, which leads to increase in parasitic power for fuel cell operations. Fig. 10 shows the effects of the inlet gas velocity on S_w, A_w, and R_{dp} in the cases where the pores in the GC are positioned at the center of the GDL surface. The instant at which the water in the channel begins to be discharged through the channel outlet is by far earlier in Case 2 than in Case 4 because of the relatively high inlet gas velocity in the former case. Although the water discharge through the channel outlet occurs along the top wall in Case 4 (Fig. 5), the S_w decrease gradient is observed to be similar to that in Case 2 (Fig. 10a). Although A_w and S_w decreased simultaneously in Case 2, the instant of S_w decrease was observed to precede that of A_w decrease in Case 4 (Fig. 10b). This is because droplets are attached to the top wall before the water discharge occurs through the channel outlet, resulting in a relatively reduced coverage of the bottom surface (Fig. 5). Moreover,

Table 5
Dimensionless numbers.

Case	$Re_{gs}\left(=\frac{\rho_{air}V_{air}D_h}{\mu_{air}}\right)$	$We_{gs}\left(=\frac{\rho_{air}V_{air}^2D_h}{\sigma}\right)$	$\mathrm{Bd}\left(=\frac{(\rho_{water}-\rho_{air})g(d/2)^2}{\sigma}\right)$
1	273.8	0.681119	0.003260942
2	273.8	0.681119	0.003279985
3	273.8	0.681119	0.003199500
4	54.8	0.027245	–
5	54.8	0.027245	–
6	54.8	0.027245	–
7	136.9	0.17028	0.006569356

(D_h: hydraulic diameter of gas channel, d: detachment diameter of droplet).

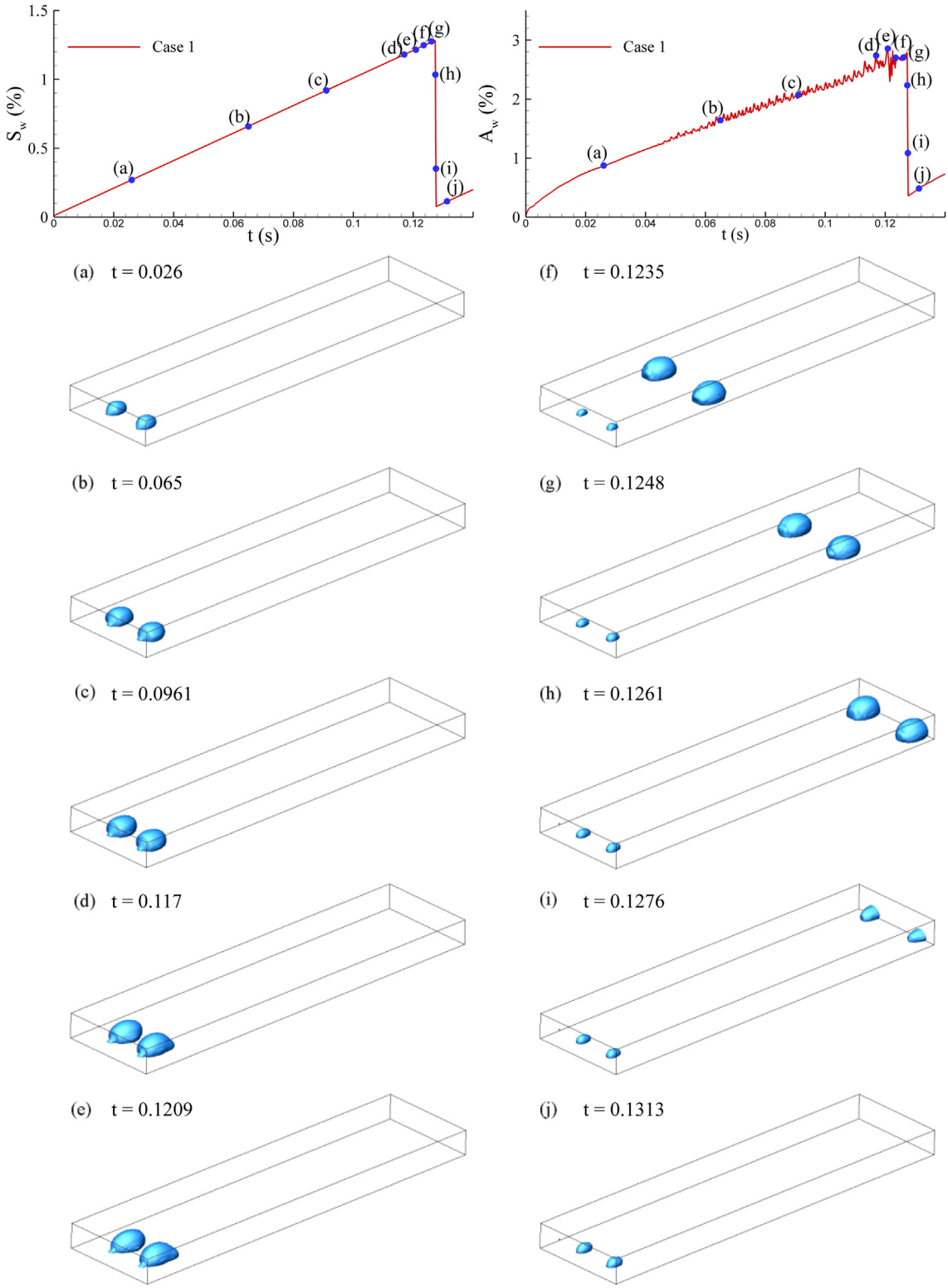

Fig. 2. Time evolution of liquid water interface for Case 1. The points in the $S_w(t)$ diagram correspond to the respective instants in the liquid water plots.

whereas R_{dp} shows a change pattern similar to that of A_w in Case 2, it continues to increase in Case 4, despite the decrease in A_w, until the water begins to be discharged through the channel outlet (Fig. 10c). On the other hand, Fig. 11 shows the effect of the inlet gas velocity in conditions where the pores in the GC are positioned near a sidewall. In Fig. 11a, it is observed that the time for the water in the channel to be discharged through the channel outlet occurs earlier in Case 3 because of its high inlet gas velocity. Nevertheless, as the water discharge through the channel outlet occurs alongside the edge in Case 5 as well as in Case 3 (Fig. 6), the gradient of S_w decrease is gradual. In Fig. 11b, the instant of A_w decrease is observed to occur earlier than that of S_w decrease in

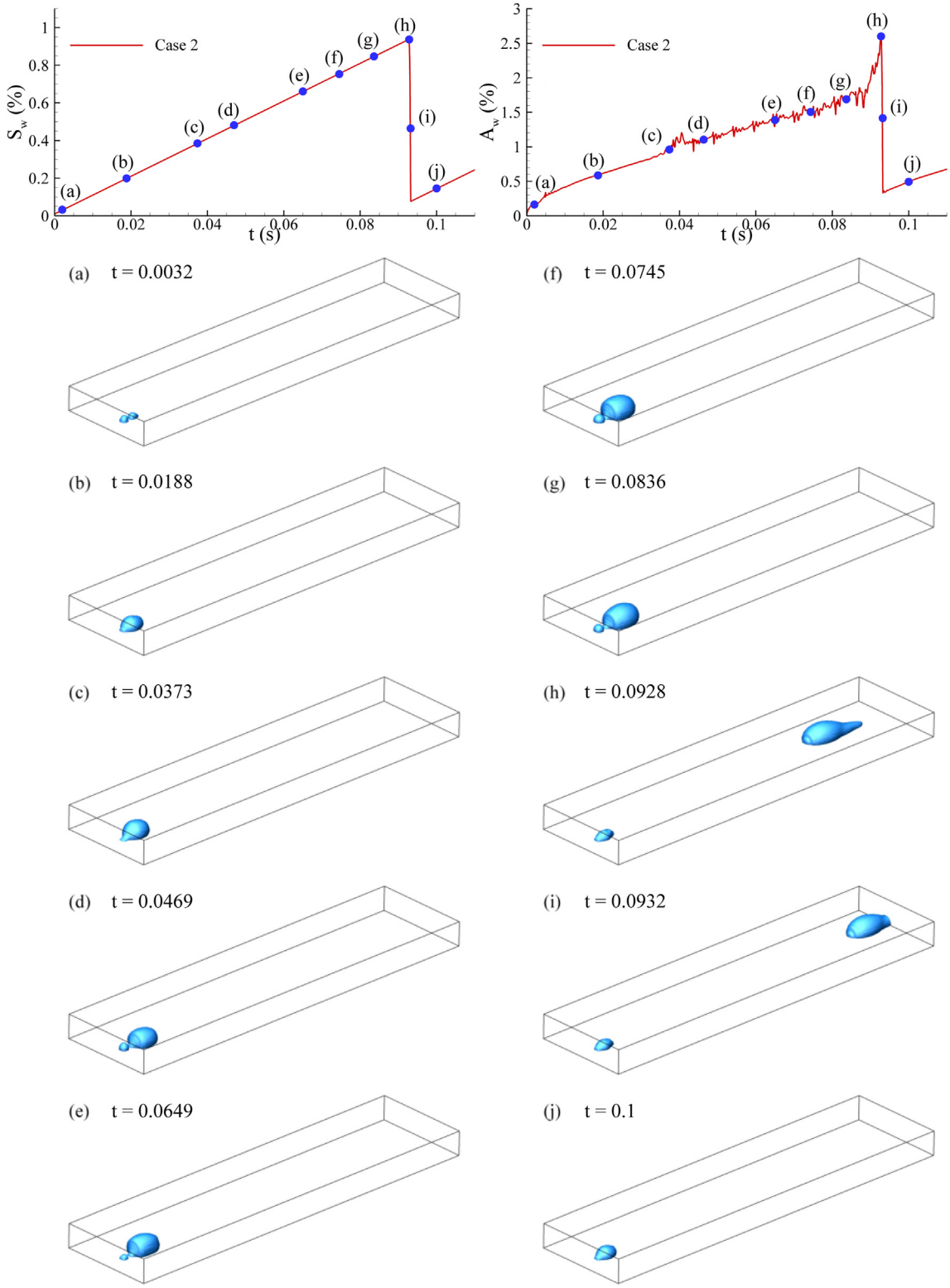

Fig. 3. Time evolution of liquid water interface for Case 2. The points in the $S(t)$ diagram correspond to the respective instants in the liquid water plots.

both Case 3 and Case 5, but A_w starts decreasing earlier in Case 5 than in Case 3 (Fig. 11b). This is because, in Case 3, droplets are attached to the sidewall after being detached from the pores before the water discharge begins through the channel outlet, whereas, in Case 5, droplets are attached to the sidewall even before their detachment from the pores (Fig. 6). The relative change in pressure drop showed a similar pattern to that of A_w in Case 3, whereas the R_{dp} in Case 5 continues to increase, following the particular repetitive increase–decrease pattern of A_w, until the water begins to be discharged through the channel outlet (Fig. 11c). The results shown in Figs. 10 and 11 demonstrate that a relatively low inlet velocity induces a condition where S_w is large,

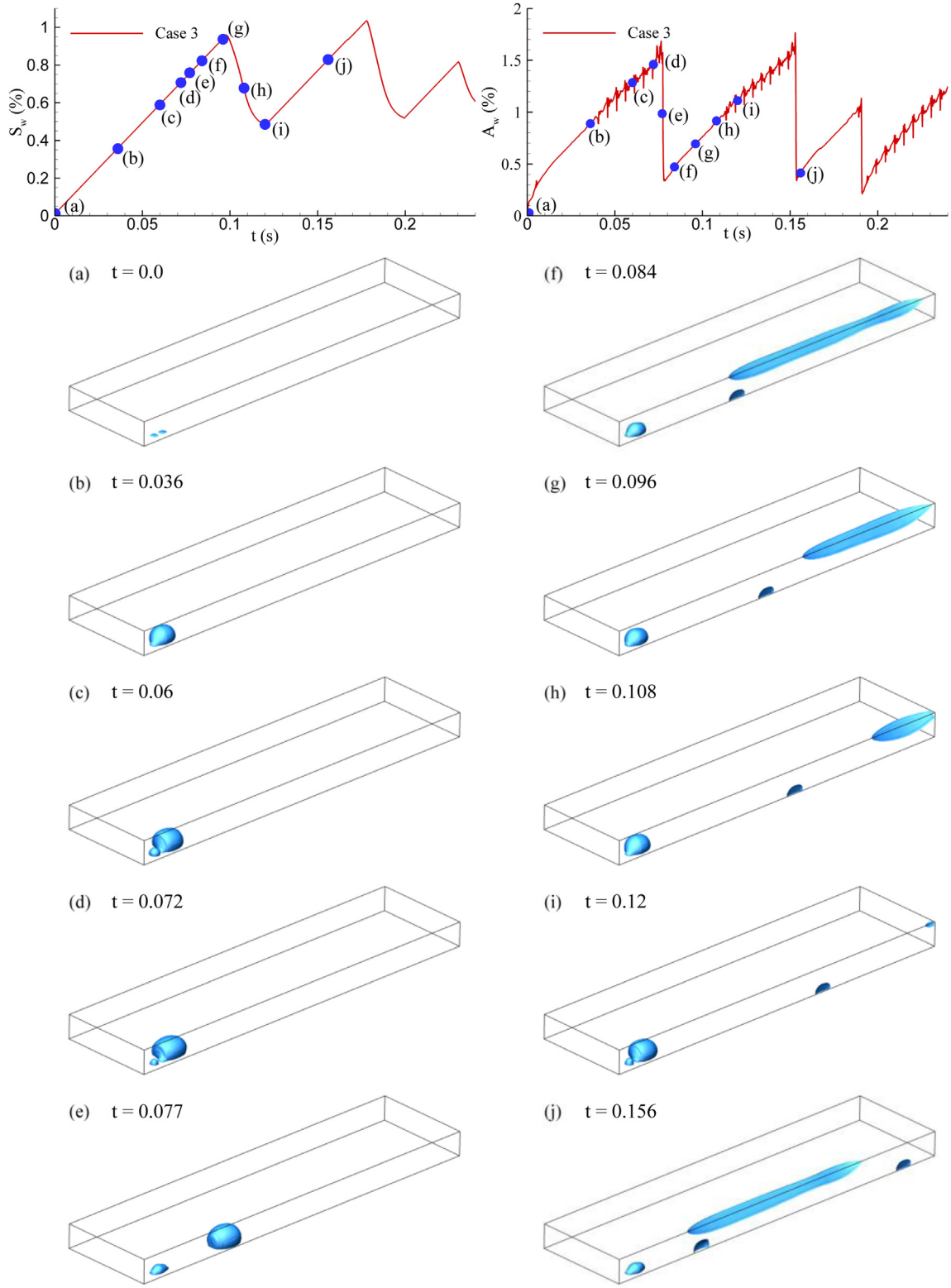

Fig. 4. Time evolution of liquid water interface for Case 3. The points in the $S(t)$ diagram correspond to the respective instants in the liquid water plots.

because of the increased droplet size, and the water discharge occurs later. Further, the comparison of the GDL surface coverage ratio A_w reveals that the water discharge through the channel edge is more effective, which is consistent with the findings of Zhang et al. [1].

In cases where the droplets growing from the pores in the GC are not detached from, but attached to, the channel wall, the water discharge is influenced by the properties of the channel wall. The effects of the sidewall contact angle on the S_w, A_w, and R_{dp} in the GC are shown in Fig. 12. If the channel wall is

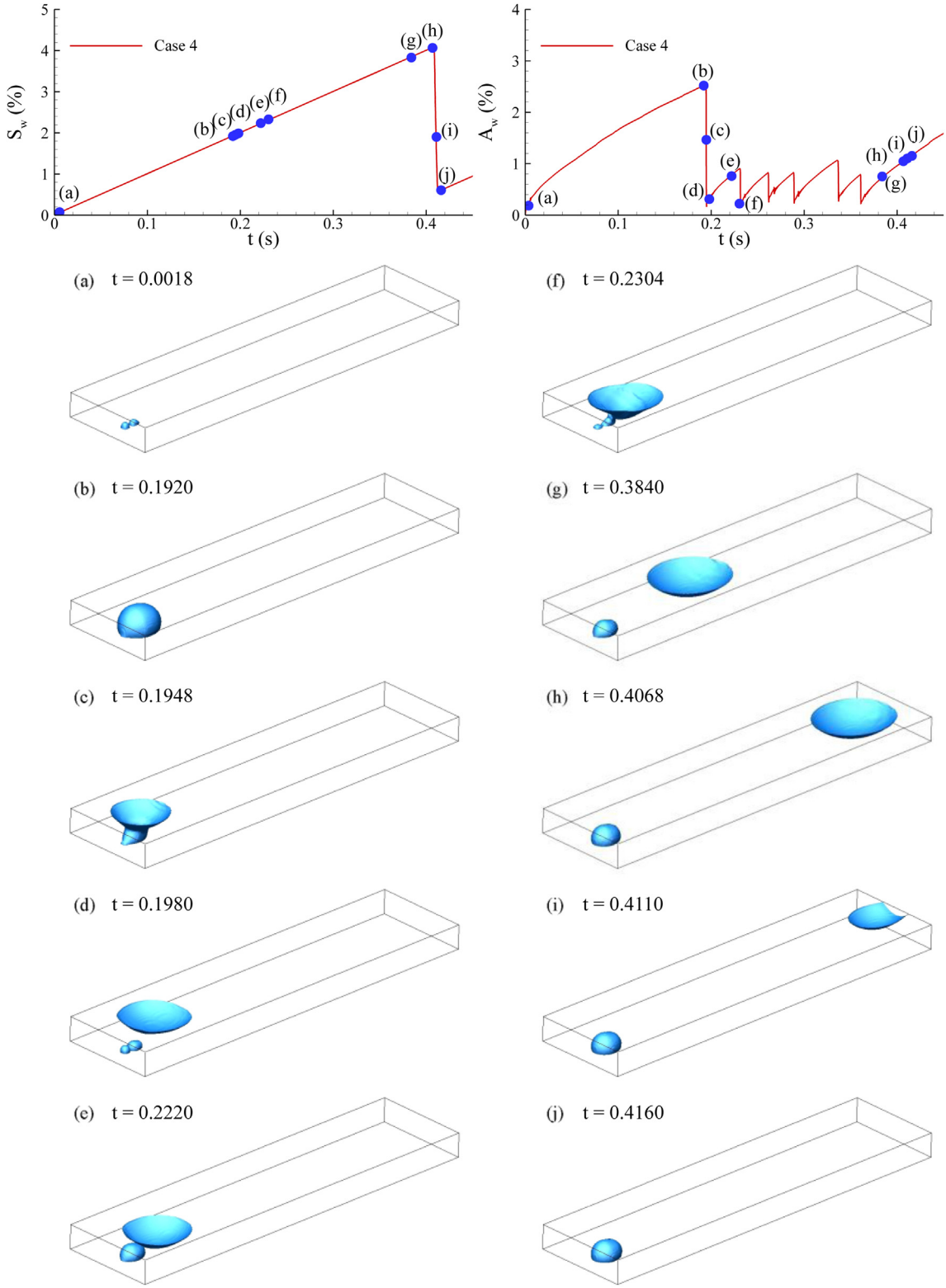

Fig. 5. Time evolution of liquid water interface for Case 4. The points in the $S(t)$ diagram correspond to the respective instants in the liquid water plots.

hydrophilic, as in Case 4, S_w increases, abruptly decreases, and then enters into a repetitive increase–decrease pattern. If the channel wall is hydrophobic, as in Case 6, S_w keeps increasing (Fig. 12a). The starting point of A_w decrease was identical in both Case 4 and Case 6 and was earlier than that of S_w decrease. It is different, however, in that A_w continues to increase after the initial decrease in Case 6. This can be ascribed to the phenomenon of clogging in Case 6 where the mature droplet is not detached after its attachment to the top wall of the channel because of the hydrophobic property of the latter (Fig. 7). This suggests that clogging occurs more easily when the channel wall surface is hydrophobic than when it is hydrophilic. Consistently, Cai et al. [7]

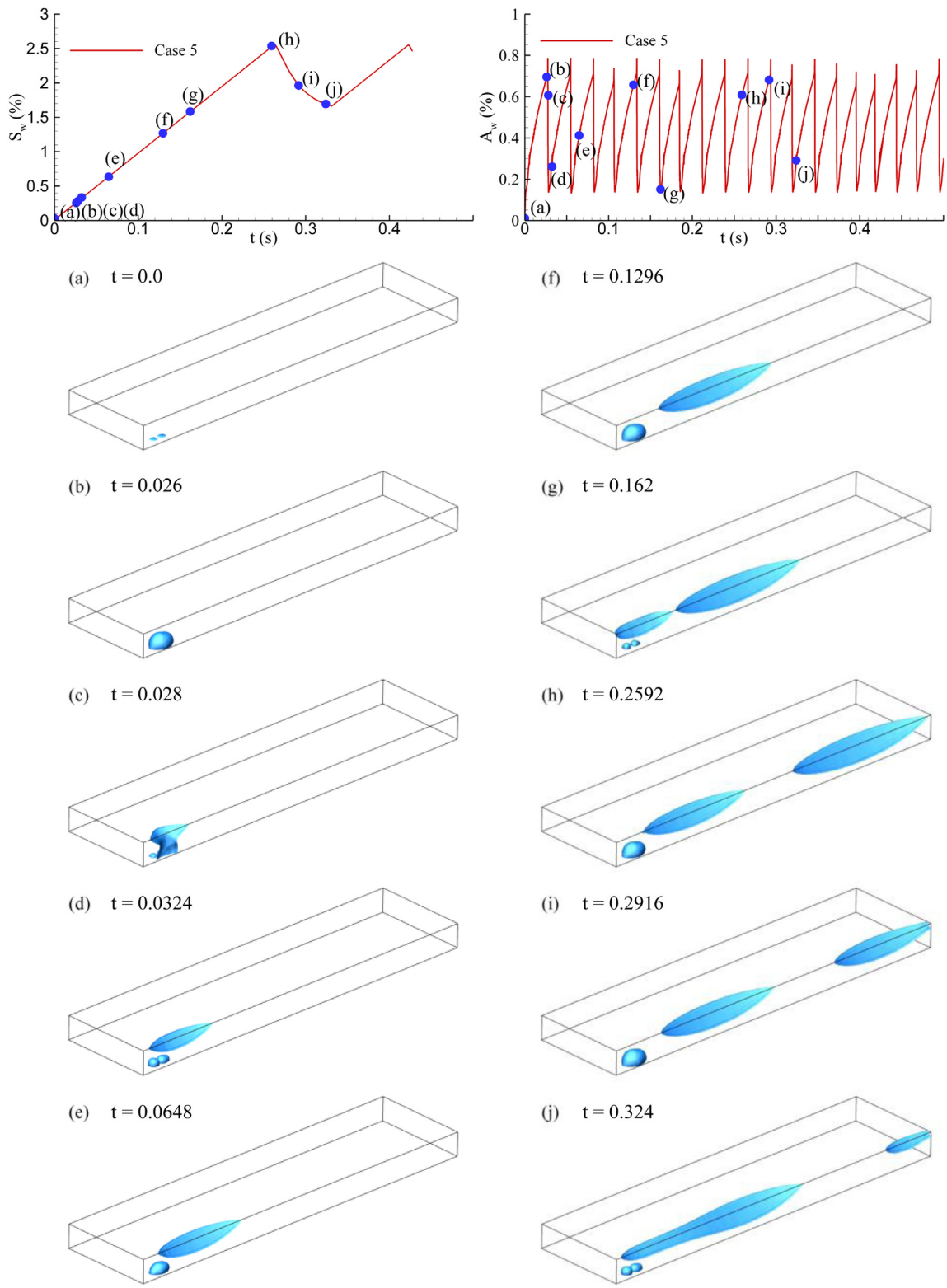

Fig. 6. Time evolution of liquid water interface for Case 5. The points in the $S(t)$ diagram correspond to the respective instants in the liquid water plots.

reported that the hydrophilic sidewall is beneficial to water discharging as well as fuel transportation from the GC to MEA. Further, the R_{dp} in Case 4 tends towards a repetitive increase–decrease pattern, whereas it continues increasing in Case 6 (Fig. 12c). Fig. 13 shows the effects of the inlet gas velocity in a hydrophobic GC. It reveals that when the gas inlet velocity is large enough, as in Case 7, the water in the channel can be easily discharged through the channel outlet (Fig. 13a). The temporal variations in A_w in Case 7 show a repetitive increase–decrease pattern similar to those in S_w because the droplets are not

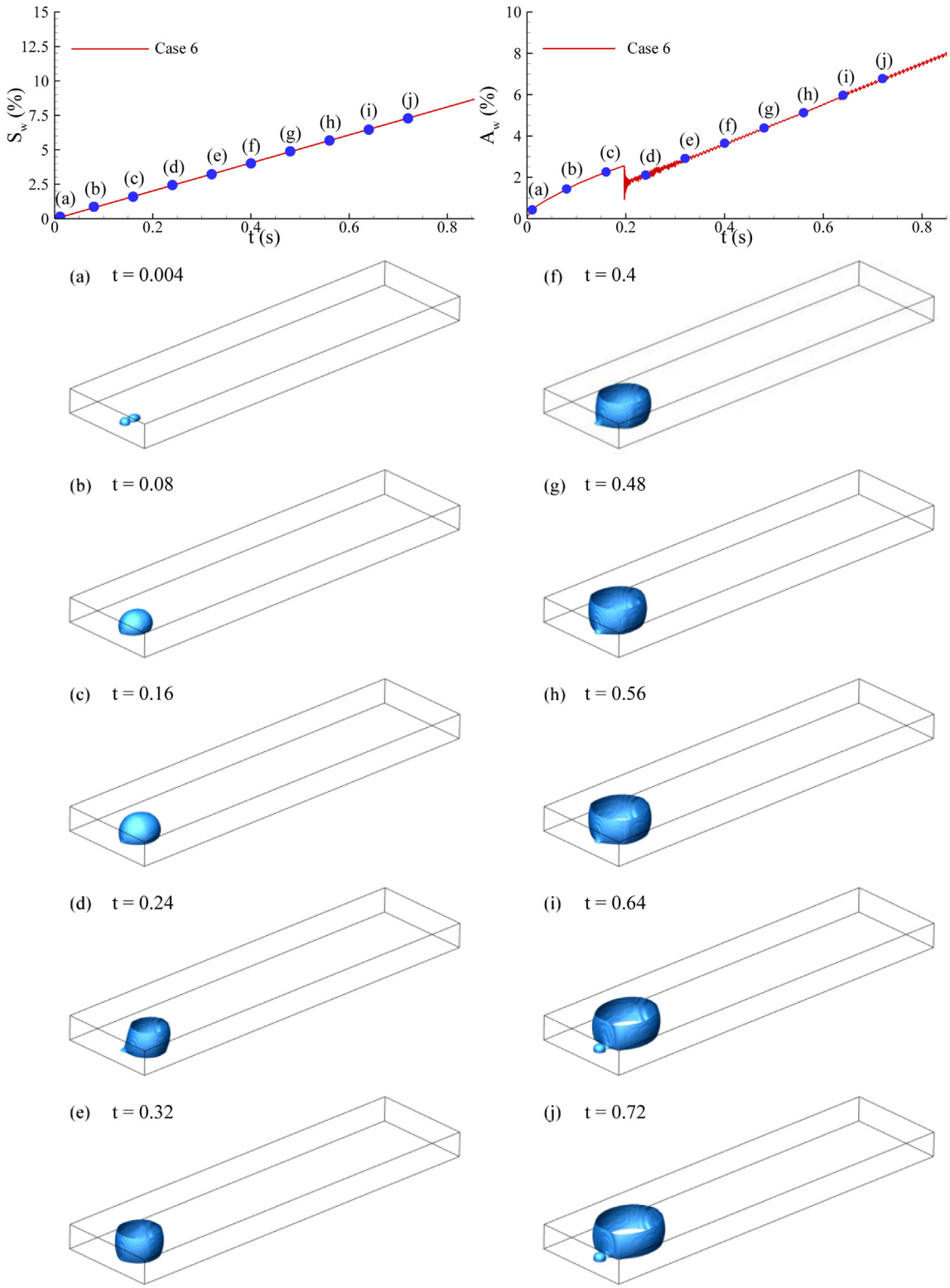

Fig. 7. Time evolution of liquid water interface for Case 6. The points in the $S(t)$ diagram correspond to the respective instants in the liquid water plots.

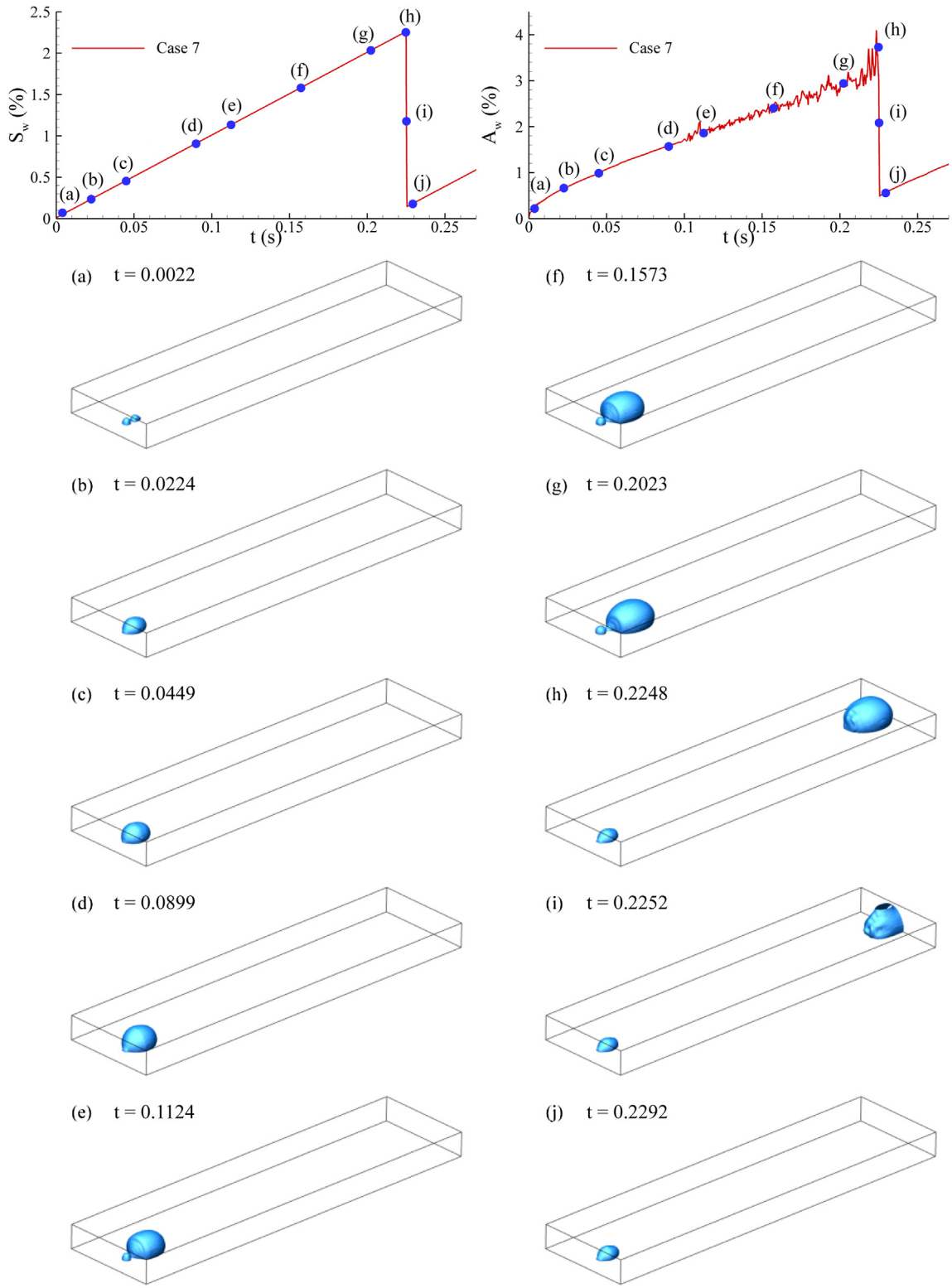

Fig. 8. Time evolution of liquid water interface for Case 7. The points in the $S(t)$ diagram correspond to the respective instants in the liquid water plots.

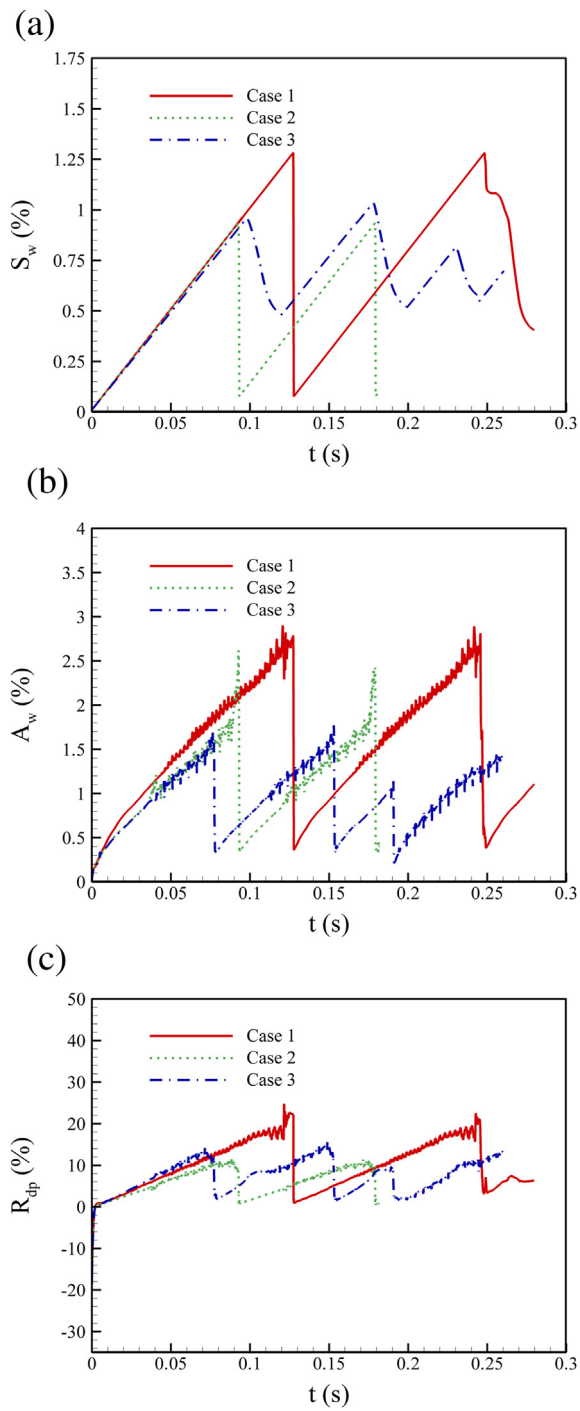

Fig. 9. Effects of pore position on the temporal variations in (a) liquid water volume fraction in the gas channel, (b) relative coverage of liquid water on the GDL surface, and (c) relative change in pressure drop along the gas channel.

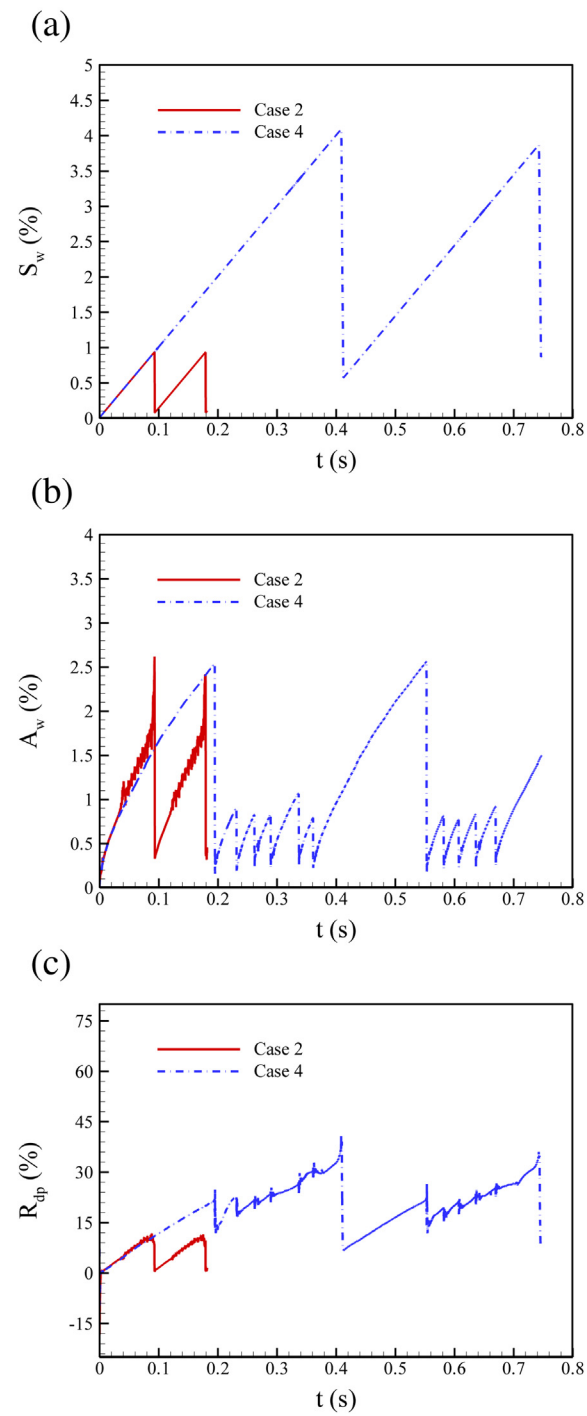

Fig. 10. Effects of inlet gas velocity on the temporal variations in (a) liquid water volume fraction in the gas channel, (b) relative coverage of liquid water on the GDL surface, and (c) relative change in pressure drop along the gas channel. Pores are located at the center of the bottom surface (Cases 2 and 4).

attached to the sidewall (Fig. 13b). Further, R_{dp}, the relative difference in the droplet-induced pressure drop, showed a pattern similar to that of A_w (Fig. 13c). These results show that when the channel wall is hydrophobic, the lower the inlet gas velocity, the higher is the chance of clogging, and the higher the inlet gas velocity, the more easily are the droplets detached from the pores, resulting in less or no clogging.

Finally, the droplet behaviors are predicted by a simple analytical approach. As the liquid water is injected from a pore, the droplets grow in time and the droplet diameter (d) can be derived as a function of time:

$$d = \left(\frac{24V_{\text{water}}A_{\text{pore}}}{\pi(2-3\cos\ \theta+\cos^3\ \theta)}t\right)^{1/3}, \tag{10}$$

where A_{pore} is the area of the pore from which the liquid water is injected. The droplet diameter measured from the present VOF

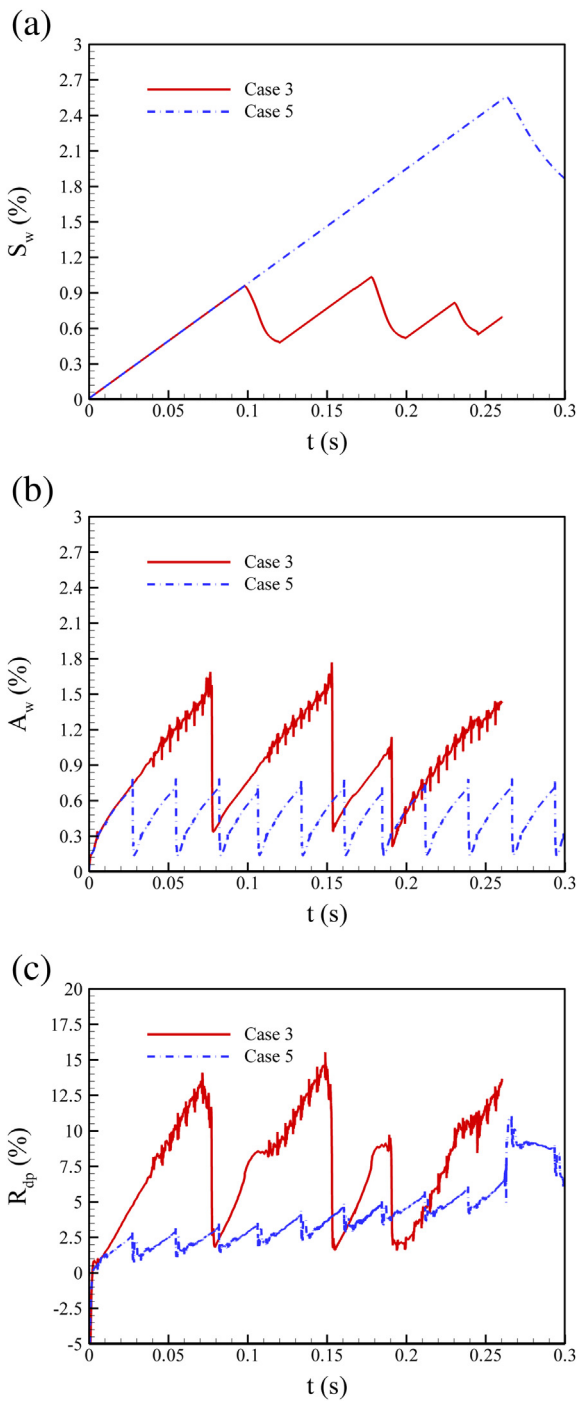

Fig. 11. Effects of inlet gas velocity on the temporal variations in (a) liquid water volume fraction in the gas channel, (b) relative coverage of liquid water on the GDL surface, and (c) relative change in pressure drop along the gas channel. Pores are located near the sidewall at the bottom surface (Cases 3 and 5).

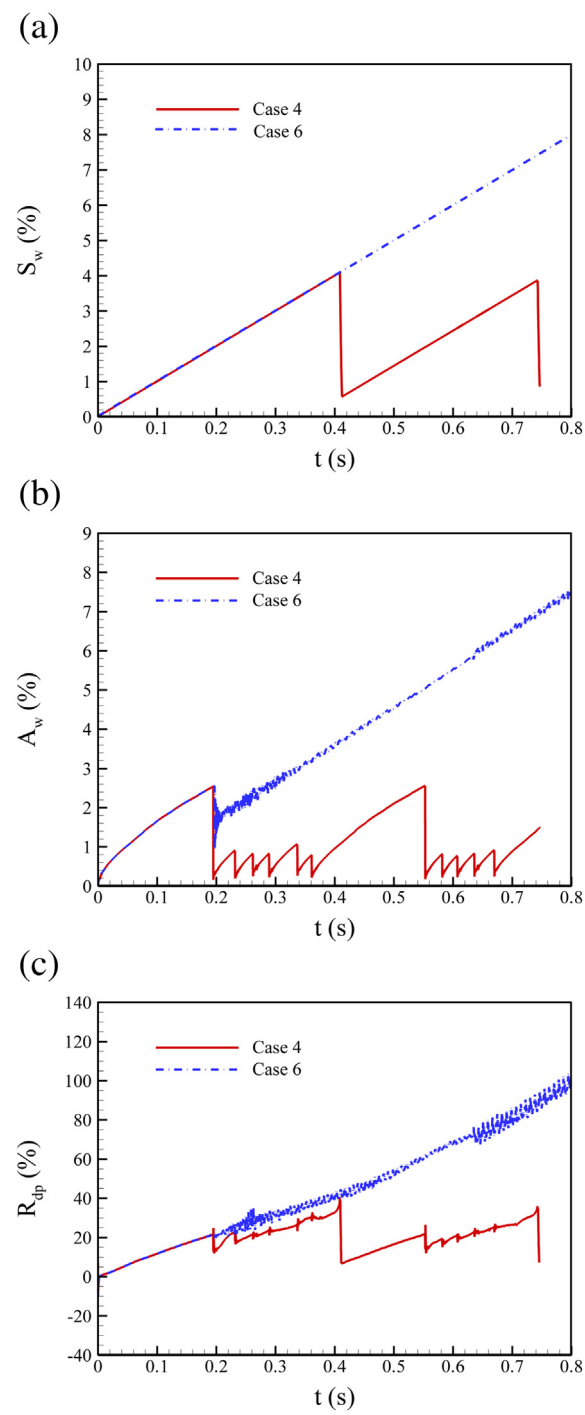

Fig. 12. Effects of sidewall contact angle on the temporal variations in (a) liquid water volume fraction in the gas channel, (b) relative coverage of liquid water on the GDL surface, and (c) relative change in pressure drop along the gas channel.

simulation is plotted in Fig. 14a together that calculated by Eq. (10). It shows that the VOF results are in good agreement with the analytical solutions.

When the surface tension force is larger than the aerodynamic drag force, the droplet will be detached from the pore. Recently, Cho et al. [10] reported new expression of drag coefficients for small droplets for typical fuel cell operation range. According to Cho et al. [10], the present study models the drag force as

$$F_d = \frac{1}{2}\rho_{\mathrm{air}} V_{\mathrm{air}}^2 A\left[46.247\left(\frac{d}{H}\right)^{0.1757}\left(\frac{\rho_{\mathrm{air}} V_{\mathrm{air}} H}{\mu_{\mathrm{air}}}\right)^{0.2158\left(\frac{d}{H}\right)-0.6384}\right], \tag{11}$$

where A is the projected area of the droplet which is estimated as $A = (\theta - \sin\theta\cos\theta)\, d^2/4$. The surface tension force can be expressed as

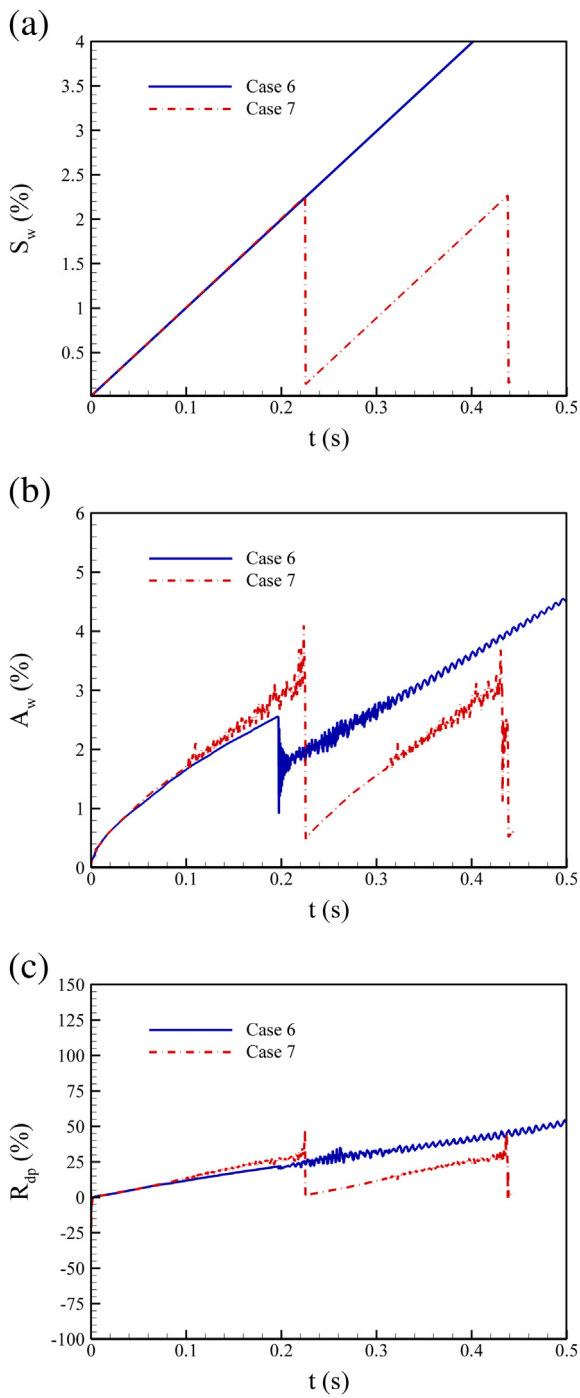

Fig. 13. Effect of inlet velocity in the hydrophobic gas flow channels on the temporal variations in (a) liquid water volume fraction in the gas channel, (b) relative coverage of liquid water on the GDL surface, and (c) relative change in pressure drop along the gas channel.

$$F_\sigma = \pi\sigma d \sin^2\theta \sin\frac{\theta_H}{2}, \tag{12}$$

where θ_H is the contact-angle hysteresis. Thus, the detachment droplet diameter (d_{detach}) can be obtained by solving $F_d = F_\sigma$.

Before the grown droplet is detached from the pore, under some conditions, it can be merged with adjacent droplets or adhere to the side or top wall of the flow channel. The criteria of droplet diameter corresponding to these different droplet behaviors can be summarized as follows:

(a) coalescence with adjacent droplet: $d > \delta_{\text{pore}}$
(b) adhesion to the top wall: $d > 2H/(1\text{-}\cos\ \theta)$
(c) adhesion to the sidewall: $d > 2\delta_{\text{side}}$
(d) detachment from the pore: $d > d_{\text{detach}}$

Here, δ_{pore} is the distance between adjacent pores and δ_{side} is the distance from the pore to the closest sidewall.

To predict the droplet behaviors based on the above criteria, the temporal droplet growth and critical droplet diameters are displayed together in Fig. 14b. The solid lines represent the temporal variation of droplet diameter and the horizontal dashed lines show the critical droplet diameters corresponding to different droplet behaviors for the flow conditions. The boxes with case number indicate the theoretically predicted droplet behavior for that case; in case 1, each droplet grows without coalescence and is detached at $t \approx 0.1$ s, whereas the droplets are merged at $t \approx 0.008$ s in the other cases (2–6). In cases 2 and 7, the merged droplet is predicted to be detached at $t \approx 0.05$ s and 0.19 s, respectively. In cases 4 and 6, it is expected that the adjacent droplets will be merged into a single droplet which continues to grow and adheres to the top wall at $t \approx 0.2$ s while the merged droplet will be attached to the sidewall at $t \approx 0.03$ s in cases 3 and 5.

The predicted droplet behaviors in Fig. 14b are well consistent with the observations in the VOF simulations excluding case 3. In case 3, the VOF simulation shows that the merged droplet is detached at $t \approx 0.07$ and immediately adheres to the sidewall, whereas Fig. 14b predicted that the droplet would be attached to the sidewall not being detached. This deviation of the prediction can be explained by considering a lateral force on the droplet due to the air velocity difference between the droplet flanks. When the droplet is located near the sidewall, the gas flow velocity over the droplet flank near the sidewall is lower as compared with the opposite side, which results in a lateral pressure force on the droplet in the direction to the channel center. Due to the lateral force, the droplet is pushed away from the sidewall and continues to grow not adhering the sidewall. Meanwhile, since the lateral pressure force increases with velocity square, when the gas flow velocity is low as in case 5, the droplet is negligibly pushed by the lateral pressure force and it grows and adheres to the sidewall as expected by Fig. 14b.

It should also be noted that the droplets are detached somewhat later in the VOF simulations as compared with the theoretical prediction. In the VOF simulations, it is observed that the grown droplet ($d > d_{\text{detach}}$) starts to move downstream at the predicted time, however, it is still connected to new small droplet emerging from the pore and thus the detachment occurs later.

4. Conclusions

During electricity generation, a polymer electrolyte membrane fuel cell (PEMFC) produces water as a byproduct in its gas channel (GC), and if the water is not adequately removed, the pores of its gas diffusion layer (GDL), or even the entire GC in extreme cases, can be blocked. Therefore, numerous studies have been conducted to improve the performance of a PEMFC by effectively removing the water generated in the PEMFC GC. In line with this, the present study was conducted by designing two pores in the same GC using a 3D volume of fluid model of a two-phase flow and carrying out a numerical simulation of droplet behaviors, wherein the pore–pore distance, GC-sidewall distance, sidewall contact angle, and air inlet velocity are varied. The main findings and conclusions of this study are summarized below:

1) The coalescence of two adjacent droplets enhanced the water removal as compared with two separate, small droplets.

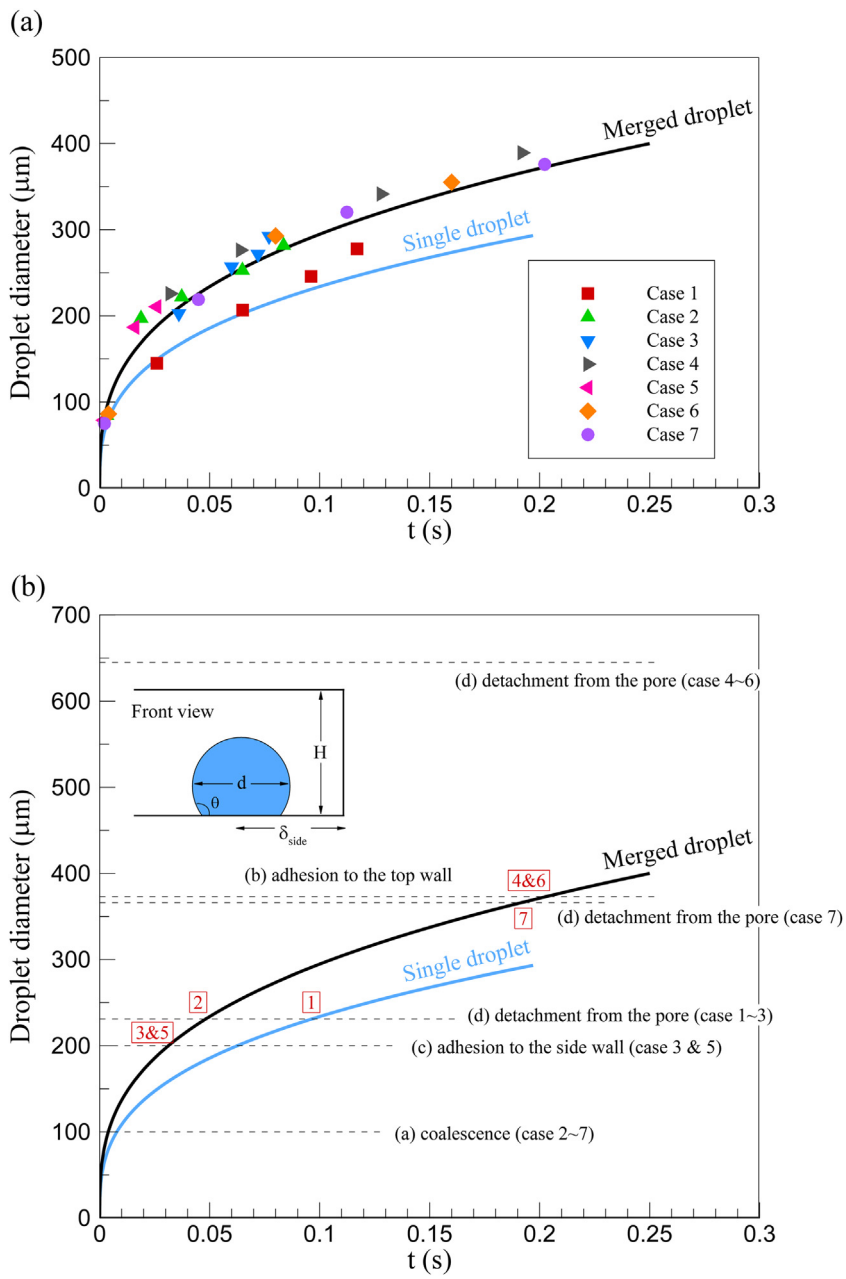

Fig. 14. Theoretical prediction of the water droplet growth in time; (a) comparison with VOF results (b) prediction of water droplet behavior.

2) If the droplet was near a hydrophilic wall surface, fuel transport was more effective because of the reduction in the GDL surface coverage despite the reduced water discharge velocity.
3) Clogging was more likely to occur when the channel wall surface was hydrophobic and the inlet gas velocity was decreased
4) Pressure drop was related more to the GDL surface coverage ratio (A_w) than to the water saturation (S_w) in the channel because it was dependent more heavily on the change in the effective surface occupied by the liquid fluid.

Acknowledgments

This work was supported by the New & Renewable Energy of the Korea Institute of Energy Technology Evaluation and Planning (KETEP) grant funded by the Korean Ministry of Knowledge Economy (No. 20103020030020).

References

[1] F.Y. Zhang, X.G. Yang, C.Y. Wang, J. Electrochem. Soc. 153 (2006) A225–A232.
[2] T. Ous, C. Arcoumanis, J. Power Sources 187 (2009) 182–189.
[3] S.-S. Hsieh, B.-S. Her, Y.-J. Huang, Energy Convers. Manage. 52 (2011) 975–982.
[4] Z. Zhan, C. Wang, W. Fu, M. Pan, Int. J. Hydrogen Energy 37 (2012) 1094–1105.
[5] T. Wu, N. Djilali, J. Power Sources 208 (2012) 248–256.
[6] N. Akhtar, P.J.A.M. Kerkhof, Int. J. Hydrogen Energy 36 (2011) 3076–3086.
[7] Y. Cai, J. Hu, H. Ma, B. Yi, H. Zhang, J. Power Sources 161 (2006) 843–848.
[8] J. Carton, V. Lawlor, A. Olabi, C. Hochenauer, G. Zauner, Energy 39 (2011) 63–73.
[9] L. Chen, T.-F. Cao, Z.-H. Li, Y.-L. He, W.-Q. Tao, Int. J. Hydrogen Energy 37 (2012) 9155–9170.
[10] S.C. Cho, Y. Wang, K.S. Chen, J. Power Sources 206 (2012) 119–128.

[11] B. Han, J. Yu, H. Meng, J. Power Sources 202 (2012) 175–183.
[12] L. Hao, P. Cheng, J. Power Sources 190 (2009) 435–446.
[13] M. Hossain, S.Z. Islam, A. Colley-Davies, E. Adom, Renewable Energy 50 (2013) 763–779.
[14] C. Qin, D. Rensink, S.M. Hassanizadeh, S. Fell, J. Electrochem. Soc. 159 (2012) B434–B443.
[15] Y. Ding, X. Bi, D.P. Wilkinson, Chem. Eng. Sci. 100 (2013) 445–455.
[16] X. Zhu, P.C. Sui, N. Djilali, J. Power Sources 181 (2008) 101–115.
[17] X. Zhu, P.C. Sui, N. Djilali, J. Power Sources 172 (2007) 287–295.
[18] K. Jiao, B. Zhou, P. Quan, J. Power Sources 157 (2006) 226–243.
[19] A.D. Le, B. Zhou, Electrochim. Acta 54 (2009) 2137–2154.
[20] A.D. Le, B. Zhou, J. Power Sources 195 (2010) 5278–5291.
[21] J.U. Brackbill, D.B. Kothe, C. Zemach, J. Comput. Phys. 100 (1992) 335–354.
[22] ANSYS FLUENT 12.0 Theory Guide, ANSYS Inc.